Edinburgh Research Explorer

An effective sphere-based model for breakage simulation in DEM

An effective sphere-based model for breakage simulation in DEM

Luís Marcelo Tavares [a], *, Victor A. Rodriguez [a], Marina Sousani [b], Carles Bosch Padros [b], Jin Y. Ooi [c]

[a] Department of Metallurgical and Materials Engineering, Universidade Federal do Rio de Janeiro – COPPE/UFRJ, Rio de Janeiro, RJ, Brazil
[b] Altair EDEM, Edinburgh, UK
[c] Institute for Infrastructure and Environment, University of Edinburgh, UK

ARTICLE INFO

ABSTRACT

Breakage occurs in several particulate systems that are simulated using the discrete element method (DEM), namely crushing and grinding as well as inadvertently in several others that include transportation, handling, mixing, separation and geotechnical applications. Different approaches may be used to describe particle breakage using DEM, but in cases in which particle breakage influences significantly the flow behaviour of the material, imbedding the breakage description in DEM provides the only valid alternative. This study describes the implementation of a detailed breakage model based on particle replacement with spheres in the commercial software EDEM. It accounts for variability and size-dependency in particle fracture energies, weakening of particles by unsuccessful stressing events, as well as addressing several reported shortcomings in sphere replacement schemes. The model is verified in great detail on the basis of single-particle breakage information and validated using measurements in unconfined particle beds of mineral ores.

© 2021

1. Introduction

The discrete element method (DEM) has reached great success in applications that range from geotechnics to process industries, giving insights into a variety of phenomena involving particulate materials. In several systems of interest, however, describing the motion and interaction of particles is not sufficient, since particles can undergo breakage. While in some systems this description can be decoupled from the DEM simulation [1–4], in others breakage must be embedded in it to achieve satisfactory predictions.

Several approaches have been successfully used over the years to describe breakage within the DEM environment, which may be classified in two groups. The first represents techniques in which parent particles are made up of primary particles that are bonded together and that are fully resolved from the beginning of the simulation. Examples of these are the bonded-particle model (BPM) [5,6] in which spheres are used; the discrete grain breakage (DGB) [7,8], the combined finite and discrete element method (FDEM) [9], the cohesive fracture model [10] and the bonded cell method (BCM) [11] which uses polyhedral cells. Additional differences among these are related to the expressions used to represent the failure criteria between individual primary particles, as

well as the type of interactions between them. Although generally valid, these approaches have limitations associated to the computational effort, since all primary particles must be resolved and interact during the entire simulation [12].

The second group, called particle replacement, is represented by techniques in which a particle is replaced by progeny particles that occupy geometrically the space of the parent particle every time a failure criterion is met. Since breakage is represented instantaneously (within the calculation cycle of one time step), new fragmentation events may occur successively if there is still energy remaining in the contact after the primary breakage event [13,14]. The progeny particles generated can be either spheres [13–19], superquadrics [20] or polyhedral cells [21–23]. Unlike the first group, there are no bonding elements in the particle replacement to represent the internal mechanical properties of the particles, making it quite versatile in relation to the implementation of different breakage models, but also critically dependent on the selection of the failure criterion. Indeed, differences among the approaches that are part of this group are often related to the failure criterion adopted and the method used to generate the size distribution of the progeny particles.

A critical issue when simulating particulate systems of interest in engineering using DEM is the computational effort, more so when breakage is embedded in the simulation. As such, it is worthwhile to focus on a breakage description that can be deployed requiring a manage-

* Corresponding author.
 E-mail address: tavares@metalmat.ufrj.br (L.M. Tavares).

able computational effort whilst maintain the fidelity in describing the physical phenomena. The convenience associated to particle replacement methods makes them an attractive option.

Spherical particles have important advantages in DEM simulation given the undisputed ease in contact detection in comparison to any other particle shape. However, two important challenges appear when using spheres associated to a particle replacement scheme in DEM. The first is either the lack of volume conservation or the excessive superposition of the fragments, since spherical fragments cannot properly fit inside a spherical parent particle. In the case when volume loss cannot be tolerated, the excessive superpositions are often dealt with by using numerical strategies to prevent explosive ejection of fragments. These strategies typically involve damping partially the unrealistic repulsive forces that appear during replacement [12]. The second limitation in particle replacement schemes is associated to the jagged and unnatural aspect of the size distribution of the fragments created. This occurs because spheres of only a few limited sizes may be used to represent a progeny size distribution [15,18].

The present work describes the adaptation of a detailed breakage model to describe breakage of brittle particulate materials implemented in the commercial code EDEM, in the form of an application programming interface (API). It resulted from a collaboration between researchers from the Federal University of Rio de Janeiro and the University of Edinburgh with the direct involvement of the engineering team from Altair EDEM. The model accounts for variability and size-dependency in breakage probability and weakening of particles by repeated stressing. By using a recently developed stochastic approach to particle replacement [24], it allows fragment size distributions to be represented with great fidelity, contrasting with previous studies [15,18] that also used spherical particle replacement but that were deterministic in nature. The implementation has been verified by comparisons to the continuum model and then validated on the basis of unconfined particle-bed experiments. Parameters and data used in the present work were essentially the same as those recently used in verification and validation of implementation of the model using polyhedral particles in Rocky DEM [23].

2. Model implementation

2.1. Critical condition for fracture

The model in question is comprised of semi-empirical and semi-theoretical mathematical expressions that describe the critical condition for failure of a particle which is instantaneously replaced by a family of spheres with smaller sizes once considered broken. Each DEM particle is assigned a value of specific fracture energy, which is the maximum magnitude of the stressing energy that the particle can sustain in an event before breaking into fragments [25,26]. Using a random number generator that draws values from 0 to 1, each particle created in the DEM simulation is assigned a value from the particle fracture energy distribution, as illustrated in Fig. 1.

The actual value of particle fracture energy that each particle will be assigned when the simulation is initialized will vary according to the upper-truncated lognormal distribution [27], given by

$$P_o(E) = \frac{1}{2}\left[1 + \text{erf}\left(\frac{\ln E^* - \ln E_{50}}{\sqrt{2\sigma^2}}\right)\right] \tag{1}$$

and

$$E^* = \frac{E_{\max} E}{E_{\max} - E} \tag{2}$$

where E is the specific fracture energy of the particle, which corresponds to the maximum stressing energy that it can sustain in a stressing event and not break, E_{max} is the upper truncation value of the distri-
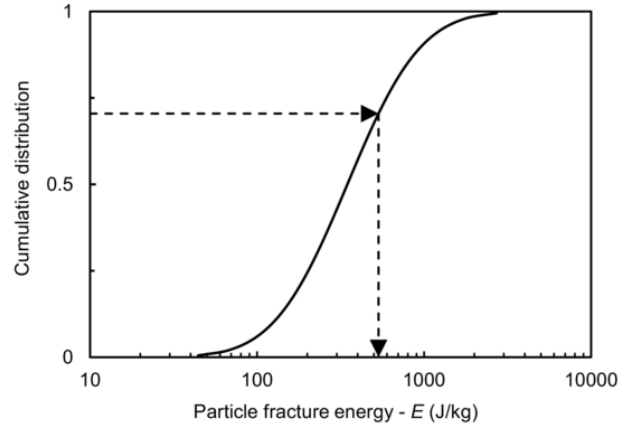

Fig. 1. Illustration of Monte Carlo sampling of particle fracture energy value from the lognormal distribution for particles contained in a given size range. The dashed line considers a drawn value of 0.71, yielding the particle fracture energy of 534.1 J/kg.

bution, E_{50} and $\sigma2$ are the median and the geometric variance of the distribution, respectively. The upper truncation value may be conveniently represented by the dimensionless ratio E_{max}/E_{50}. All values may vary as a function of particle size, but within an order of magnitude in particle size, both $\sigma2$ and E_{max}/E_{50} can be assumed, for simplicity, to remain relatively constant [26] and be fitted to experimental data.

It is known that the strength of a brittle material varies with particle size, so that as particle size reduces the energy per unit mass required to break a brittle particle increases [25,26,28]. This effect is accounted for in the proposed model in the variation of E_{50} using a semi-empirical expression inspired in reliability theory [26,29], given by

$$E_{50,i} = \frac{E_\infty}{1 + k_p/k_s}\left[1 + \left(\frac{d_o}{d_i}\right)^\varphi\right] \tag{3}$$

where E_∞, d_o and φ are model parameters that must be fitted to experimental data and d_i is the representative size of particles contained in size class i. This expression allows representing the power-law increase in median fracture energies as particle size reduces as well as the reach of a relatively constant value for coarser particles, as often observed empirically [26,29]. The parameters k_p and k_s are, respectively, the Hertzian stiffness of the particle and of the surface of the device used in measuring the breakage characteristics, where $k_s = Y/(1 - \nu^2)$, where Y is the Young's modulus and ν the Poisson's ratio. Since the surface of the device is typically steel [26,29], then k_s is approximately 230 GPa.

The critical condition for fracture of each individual particle is initialized at the beginning of the simulation using the model parameters evaluated from the single particle breakage tests [26], Eqns. (1)–(3) and the Monte Carlo scheme illustrated in Fig. 1. This approach is also used every time a particle is created, such as when a parent particle is replaced by newly created progeny. As such, one important assumption in the model is that the progeny does not inherit any information from the parent particle, so that the fracture energy of each progeny fragment depends only on its size (Eq. 3). The validity of this assumption is yet to be demonstrated empirically.

When simulation begins the energy involved in each stressing event is calculated at each time step as the summation of the elastic and the dashpot energy in the Hertz-Mindlin contact model, using the approach discussed in 2.3. The proportion e of this energy that is allocated to the particle and is available for breakage is estimated on the basis of the elastic constants of the bodies in contact and is given by the Hertz contact theory [30,31]

$$e = \frac{k_m}{k_p + k_m} \tag{4}$$

where k_p and k_m are the Hertz contact stiffnesses of the two contacting bodies [26]. A derivation of this equation is presented in Appendix A. In the case of a particle-wall contact, k_m is the Hertzian stiffness of the surface in contact with the particle. In the case of a stressing event involving two particles of the same material, Eq. (4) gives $e = 0.5$, since the energy will be equally split between them.

If the maximum energy available E_k' to the particle in a stressing event is smaller than the fracture energy of the particle, the particle will not undergo breakage, but may sustain internal damage, which will make it more amenable to break in a future stressing event. This weakening is described with a model based on continuum damage mechanics [32], through which the specific fracture energy of the particle will be reduced to [27,33]

$$E' = E \ (1 - D) \tag{5}$$

where E' is the specific fracture energy of the particle after a stressing event and D is the damage parameter, which is given by [27,33].

$$D = \left[\frac{2\gamma}{(2\gamma - 5D + 5)} \frac{E_k'}{m_p E} \right]^{\frac{2\gamma}{5}} \tag{6}$$

where γ is the damage accumulation coefficient, which characterizes the amenability of a material to sustain damage prior to catastrophically breaking, E_k' is the energy in the stressing event available to the particle and m_p the particle mass. γ is the only parameter in the model, which must be fitted on the basis of data generated by impacting particle repeatedly at the same stressing energy [27,33]. D is implicit in Eq. (6), so that the equation should be solved iteratively from an initial guess of $D = 0$ [27]. Eqns. (5) and (6) are only computed whenever a contact has ceased and the particle has not undergone breakage, so that E_k' is the maximum value of stressing energy the particle is subjected to during the compression part of the collision event.

The only piece of information stored individually in the simulated particles, besides size, is their specific fracture energy, which reduces according to Eq. (5) as particles undergo unsuccessful stressing events. Being a Markovian process [34] in which the system depends only on its current state for predicting the simulation outcome, it minimizes the demand for storing information.

The energy-based criterion for fracture used in the present model makes it far less sensitive than a force or stress-based model to the choice of the absolute value of the contact stiffness in a DEM simulation, since the later would change significantly in case the user reduces the Young's or the shear modulus so as to accelerate simulations in DEM.

Although the breakage probability and weakening model were originally developed in the form of continuous distributions, being particle-based, they are directly applicable to describe populations of discrete particles in DEM.

The validity of Eqns. (1)–(7) in describing the critical condition for fracture has been demonstrated from breakage testing of single particles of a variety of brittle materials [26,27,29,31,33,35].

2.2. Particle replacement

Whenever the specific energy in a stressing event E_k'/m_p that is available to a particle is higher than its specific fracture energy, it breaks and is replaced by its fragments. Unlike the breakage probability presented in the previous section, adapting a continuous breakage distribution model to a discrete breakage event is far more challenging, since the original model was developed on the basis of average information on fragments distribution as well as on median values of fracture energies of particles.

The extent of breakage into fragments may be characterized using a single parameter, t_{10}, which represents the proportion of fragments that

are finer than 1/10th of the parent particle size [33,36]. Tavares [33] proposed that the extent of breakage when stressing a batch of particles is related to the specific stressing energy and to the median fracture energy of the particles through the expression

$$t_{10} = A \left[1 - \exp\left(-\frac{b' E_k'}{m_p E_{50b}} \right) \right] \tag{7}$$

where A and b' are model parameters fitted to experimental data, in which A corresponds to the maximum value of t_{10} that can be achieved when breaking a material in a single stressing event, and E_{50b} is the median specific fracture energy of particles that underwent breakage. For instance, in Fig. 1, particles in a sample are each subjected to a single impact at 534.1 J/kg, resulting in breakage of 71% of them, E_{50b} would be equal to 258.0 J/kg, which is the 35.5th percentile of the distribution. This value is lower than 347.3 J/kg, which is the value of the median of the original distribution. The higher the energy E_k' in comparison to the median fracture energy of the particles, the higher the value of t_{10} and the finer the progeny size distribution. By using the median specific fracture energy of the particles that underwent breakage, Eq. (7) is able to account for the particle size effect in breakage [33].

When adapting Eq. (7) to describe individual particles, it has been proposed to replace E_{50b} by the fracture energy of each particle [23,24]. As such the t_{10} value from breakage of an individual particle, now identified as t_{10}', is given by [24]

$$t_{10}' = A \left[1 - \exp\left(-\frac{b' \kappa E_k'}{m_p E} \right) \right] \tag{8}$$

Values of κ were found to vary from about 0.95 to $\exp(\sigma^2/2)$. For high values of $E_k'/(m_p E)$, σ and E_{max}/E_{50}, the value of κ may not be close to one and empirical expressions were proposed elsewhere [24] to estimate it.

When a particle is stressed with the minimum amount of specific energy required for breakage ($E_k'/m_p = E$), then Eq. (8) becomes

$$t_{10}' \cong A \left[1 - \exp\left(-b' \right) \right] \tag{9}$$

Eq. (9) thus defines the minimum value of t_{10} that can occur when breaking a particle of a given material, which is called primary particle breakage [37]. From values of parameter A and b' from previous studies [26,29,38], values of t_{10}' range from 0.6% to approximately 6%. In practice, Eq. (8) is used at all times in the simulations involving discrete particles.

Application of the present model to accurately simulate breakage of spherical particles in DEM requires the definition of the progeny size distribution in which a parent particle will be replaced. Carvalho et al. [39] described successfully breakage of single particles empirically using the incomplete beta function, given by

$$t_n = \frac{100}{\int_0^1 x^{\alpha_n - 1} (1 - x)^{\beta_n - 1} dx} \int_0^{t_{10}/100} x^{\alpha_n - 1} (1 - x)^{\beta_n - 1} dx \tag{10}$$

where the cumulative mass of particles passing (t_n) a screen with size equal to 1/nth of the parent particle is calculated using the t_{10} or the t_{10}' value. In the model two parameters (α and β) must be fitted to each value of n selected. Therefore, with the seven n values (1.2, 1.5, 2, 4, 25, 50 and 75) a total of 14 parameters must be fitted from the measurement data. From Eq. (10) and a given value of t_{10}, the various t markers ($t_{1.2}$, $t_{1.5}$, t_2, t_4, t_{25}, t_{50} and t_{75}) are estimated, from which the progeny size distribution down to a size of 1/75th of the parent size can be reconstituted [36]. Although parameters in Eq. (10) may be estimated for each particular material of interest [24,36,39] a set of values that were found to be able to describe well data from 40 materials, in-

cluding various rocks, ores and cement clinkers, has been compiled in Table 1 [24].

In order to adapt this model to discrete particles, Tavares and Chagas [24] proposed an approach that combined the generation of standard families of discrete fragments for each value of t_{10}' and a Monte Carlo simulation scheme to select which of the families are drawn when a particle breaks. The standard families, generated using a procedure detailed in [24] on the basis of the parameters in Table 1, were found to be valid for a variety of materials. In this approach, fragments making up the original volume of the parent particle are created following a $\sqrt[4]{2}$ size series. For instance, in order to accurately represent the progeny size distributions observed from experiments in a drop weight tester, no more than 11 families were required for each t_{10}' value [24]. The domain of t_{10}' values of interest for each material ranges from the value given by Eq. (9) to the maximum value given by parameter A. However, being a continuous variable, infinite values can appear, so that the value corresponding to a given set of families for a particular t_{10}' must be selected from the one that more closely matches the result from Eqns. (8) or (9). An example of a set of families for a particular value of t_{10}' is given in Table 2, whereas tables containing families for several other t_{10}' values are available elsewhere [24].

Fig. 2 compares the size distributions from the families presented in Table 2. It shows that they are scattered around the sought size distribution, where the latter has been obtained from interpolation of the values from Eq. (8) for the various n values. It also shows that the individual size distributions are jagged as can be expected given the limited number of progeny fragments involved in each replacement.

When applying this approach in the event that a particle breaks with a particular value of t_{10}', one of the families are drawn randomly – accounting for its respective probability given in Table 2 – and the sizes of fragments assigned by multiplying the values of relative fragment size x_i by the parent particle size. Tavares and Chagas [24] demonstrated

Table 1
Optimal parameters of the incomplete beta function for a total of 40 materials, including ores, rocks and cement clinkers [24].

n	α_n	β_n
1.2	0.448	10.508
1.5	0.706	7.913
2	0.959	5.780
4	1.105	2.619
25	0.981	0.524
50	0.956	0.339
75	0.934	0.255

Table 2
Families of fragment size distributions that could be drawn in particle replacement for $t_{10}' = 3.0$.

Relative particle size x_i (−)	Family of progeny spheres						
	1	2	3	4	5	6	7
1.000	0	0	0	0	0	0	0
0.841	1	1	0	0	1	1	1
0.707	0	0	2	1	0	0	0
0.595	1	0	0	2	1	1	0
0.500	0	2	1	0	0	0	2
0.420	1	0	1	1	1	1	1
0.354	1	1	0	1	1	0	0
0.297	0	1	1	2	1	2	0
0.250	1	2	0	0	0	1	2
0.210	1	1	2	0	1	1	1
0.210[a]	5	5	5	6	4	5	4
Probab. (%)	34	27	23	9	5	1	1

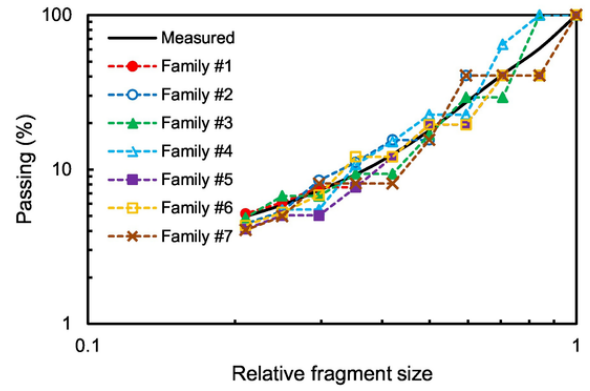[a] 'Dummy' particle size class, corresponding to particles with relative size below 0.210.

Fig. 2. Comparison of distributions in Table 2 for $t_{10}' = 3\%$ with the measured cumulative mass distribution.

that the sought size distribution is quickly approached after drawing only a few of these individual discrete distributions.

One additional feature of the approach presented in [24] is that while all fragments are represented as spheres, with relative diameters (x_i) (Table 2), every time a parent particle is replaced, a part of the spherical particles contained in the finest size class is actually meant to represent particles that are finer than x_{min}, which could not be resolved in the simulation. This minimum size of fragment replaced in each event was selected as approximately 1/5th ($x_{min} = 1/2^{9/4th}$ or 0.21) of the original particle diameter [24], in order to limit the computational effort. This results in each event having a fraction smaller than x_{min} which will not be resolved further. This fraction, termed ´dummy` size, will continue to be tracked to achieve conservation of mass. It represents the ´pan` in cumulative size distributions by sieving such as those in Fig. 2. Given this definition and the fact that these fines could not be represented explicitly in the simulation but their size distribution could be estimated using Eq. (10) from the t_{10}' value of the stressing event that was responsible for its generation, an approach has been proposed to extend the size distribution down to unresolved sizes. Therefore, once the simulation is completed and considering the breakage intensity of the event, represented by Eq. (8), the mass of dummy particles is transformed to the equivalent size distribution of the unresolved fines. Since the fines tail of cumulative size distributions from particle breakage often approaches a straight line in log-log axes [24], the Gaudin-Schuhmann equation is used [40]. As such, the fragment size distribution of the unresolved fines from each particle replacement event is described by

$$B(x) = \left(\frac{x}{x_{\min}} \right)^{\lambda} \text{ for } x < xmin \quad (11)$$

where x is the relative fragment size, $B(x)$ is the proportion of particles corresponding to the unresolved fines with relative size below x and $B(x_{min}) = 1$. Tavares and Chagas [24] suggested that the exponent λ can be estimated by

$$\lambda \cong 0.789 \log \left(\frac{t_4}{t_{75}} \right) \quad (12)$$

where both t_4 and t_{75} are a function of t_{10}' (Eq. 12).

Whenever comprehensive enough breakage data are available λ may be estimated from the values modelled for the material of interest [24]. Fig. 3 shows the significant variation of this parameter as a function of t_{10}' for different materials. When such comprehensive breakage data are not available, an option is to use average data from Table 1 [24], also shown in Fig. 3.

The fragment size distributions for a single stressing event, including the unresolved fines extension estimated on the basis of the proce-
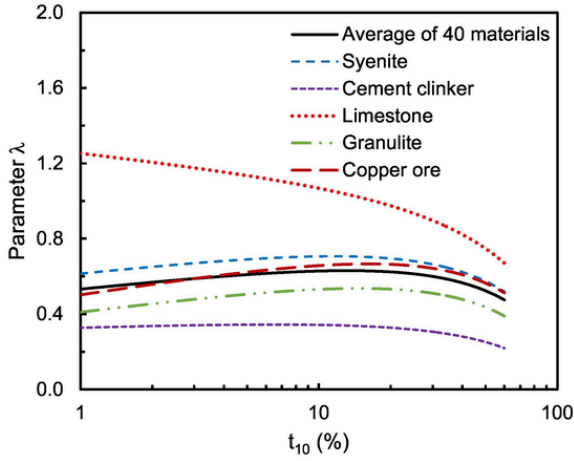
Fig. 3. Variation of exponent in Eq. (11) as a function of t_{10}' value for an average distribution for 40 materials [24], as well as for selected materials.

dure described above, are compared to the weighted average distributions for selected values of t_{10}' from Eq. (10) in Fig. 4 [24]. The good agreement shows that the proposed approach describes the analytical model very well, thus demonstrating its validity in describing a single replacement event.

While Figs. 2 and 4 represent a single replacement event, in practice particles usually undergo several sequential breakage events, even in a single impact, through which not only the parent particle, but also its progeny are replaced [37]. This is directly simulated in the proposed particle replacement approach where each fragment generated can be replaced if stressed beyond its fracture energy, with the exception of particles contained in the ´dummy` size. Naturally, uncontrolled application of this approach would lead to generation of exceedingly fine progeny fragments, which would add considerable computational cost. To limit this, another size, called global minimum size (d_{min}), is defined prior to initiating a simulation, representing the minimum size of resolved particles in the entire simulation.

The approach described above results in the appearance of a third class of fragment, besides the resolved breakable particles and the ´dummy` particles. This class of particles is called resolved unbreakable particles (Fig. 5). Since they are not allowed to break and be replaced by their progeny explicitly in a DEM simulation, the approach that is adopted starts with recording the value of t_{10}' of the first stressing event after its creation using Eq. (8). This information is stored in the particle
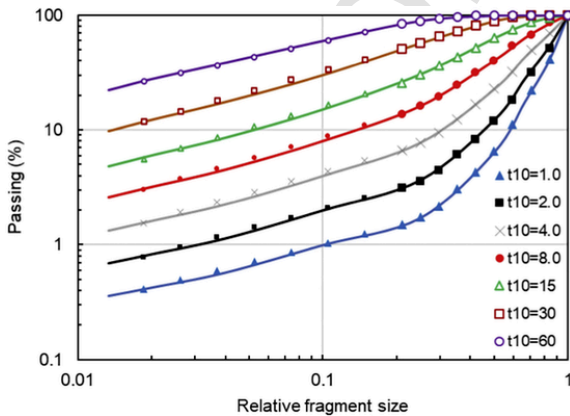

Fig. 4. Comparison of size distributions using data from 40 materials [24] for selected t_{10}' values to average distributions (large symbols), including the fines extension at relative sizes below 0.21 (small symbols), using Eq. (11), while lines represent the incomplete beta function (Eq. 10) with parameters given in Table 1.

and, after simulation is complete, the particle volume is replaced by the corresponding size distribution, described using the incomplete beta function (Eq. 13), given by [38].

$$B(x) = interp\left(t_{10}, x\right) \tag{13}$$

In analogy to the ´dummy` particles, the average model parameters given in Table 1 and the incomplete beta function (Eq. 10) can be used to generate the size distribution in Eq. (13). On the other hand, if detailed breakage data are available for the material in question that allow estimating parameters of Eq. (10), they should be rather used to describe breakage of these resolved unbreakable particles.

Upon completion of a simulation, the entire size distribution can be computed by combining the size distribution of the resolved breakable particles with that of the unresolved particles using Eq. (11) and of the resolved unbreakable particles using Eq. (13).

It is important to emphasize that the model implemented only describes massive or body breakage (when there is at least 10% mass loss of the particle) and not surface breakage. This is evident from Table 2, in which the minimum extent of breakage simulated corresponds to loss of 41% in mass of the parent particle, since the coarsest fragment considered in the simulations represents only 59% of the volume of the parent particle.

The validity of Eqns. (7), (8), (10) to (13) in describing fragment size distributions from breakage of a variety of brittle materials in single-particle breakage tests has been demonstrated in several studies [26,33,40]. Nevertheless, the model does not account for effects that are known to influence progeny distribution, such as the geometry of the impacting surface and the stressing velocity [26].

2.3. DEM model implementation

The model equations presented in 2.1 and 2.2 have been implemented in association to the Hertz-Mindlin contact model, which was used in computing the normal and tangential components of the contact force. Both normal and tangential forces have damping components where the damping coefficient is related to the coefficient of restitution. In addition, the tangential force is limited by the Coulomb law with the coefficient of static friction. The equations for these elastic spring-dashpot with a frictional slider can be found elsewhere and will not be repeated here [41,42].

The total energy available for breakage of a particle E_k' in a time step t of a DEM simulation is computed from the combination of the energy associated to the normal (E_n) and the shear (E_s) components of each stressing events to which the particle is simultaneously subjected to, giving

$$E_k' = \Sigma e E_n + c_s \Sigma e E_s \tag{14}$$

where c_s is a constant that defines the fraction of the shear energy that arbitrarily contributes to the stressing energy [35]. The use of the constant c_s multiplying the shear energy component reflects the frictional mobilization. This is associated to the fact that, on impact, a normal impact force F_n can be expected to arise directly from the normal velocity. However, the mobilization of tangential force F_t is governed by contact friction and is limited by the dynamic coefficient of friction between the impacting surfaces which in turn affects the shear energy component, hence the tangential energy contribution E_s is multiplied by the coefficient c_s to reflect this frictional mobilization.

Each component of the stressing energy is computed only when particles are being compressed. The normal component is calculated incrementally at each time step t as

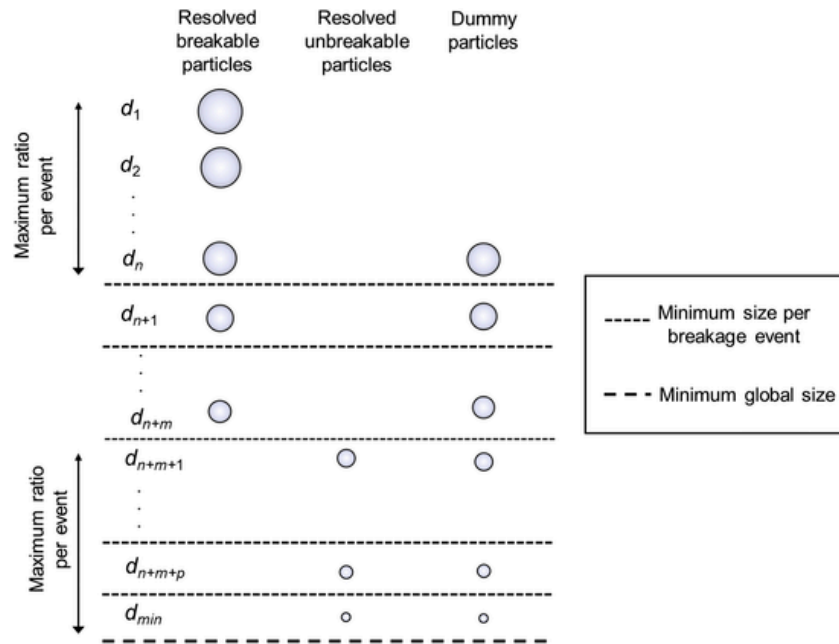$$E_n = \left(E_n\right)_{t-1} + \left(\Delta E_n\right)_t \tag{15}$$

Fig. 5. Illustration of size classes of particles (d_i) that may appear in a simulation using the proposed particle replacement approach.

where ΔE_n is the increment of normal energy. It is computed at each time step t from the product of the sum of the elastic and the dashpot forces and the increment of the normal component of the overlap $\Delta\delta_n$, being given by

$$\Delta E_n = \left(F_n^{'} + F_n^{d} \right) \bullet \Delta\delta_n \tag{16}$$

where $F_n^{'}$ is the elastic and F_n^{d} is the dashpot force at each time step. The shear component is calculated with expressions that are analogous to Eqns. (15)–(16) but are omitted for brevity. As such, the sum of the elastic and dashpot components is used to compute the stressing energy because the breakage model, given by Eqns. (1)–(10), has been fitted on the basis of experimental data where the input energy is varied.

In the implementation of the proposed approach in EDEM, particles contained in the finest ´dummy` size class are not allowed to suffer breakage. In addition, since these particles represent the fines, they can also be considered to be more deformable than particles contained in the remaining size classes, hence a lower value of stiffness may be used. This can be done by assigning a lower stiffness value to this particular size class through the interface. This would be particularly beneficial in the case of simulating breakage in confined beds, where such particles would not contribute as readily to the raise of stresses in the system.

Two additional aspects remain regarding the creation of the progeny particles. The first deals with the configuration of the fragments inside the parent particle and the second with the management of the interactive forces associated to them.

In order to resemble the outcome of a real breakage event, in which the fines are concentrated close to the point of application of stresses, spheres inside the parent particle are arranged so that the larger fragments overlap in perpendicular direction to the stress that caused breakage. The remaining finer fragments are then arranged in the leftover voids, often also overlapping with the coarser fragments, as illustrated in Fig. 6.

The progeny particles created are allowed to overlap initially to fit inside the original parent particle volume. Such overlap can be significant. For instance, consider family #7 in Table 2, in which the two largest fragments predicted by the model would require a parent particle with over 40% larger diameter to fit if no overlapping is used. There have been different approaches in the past that aimed to allow such large artificial overlaps without generating explosive forces in the
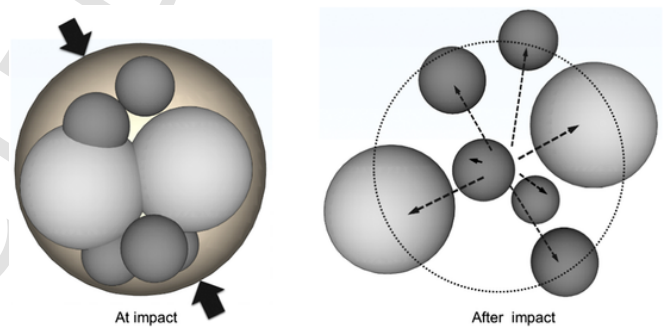

Fig. 6. Illustration of particle replacement scheme involving spheres.

packed particles. An example of which is the use of a relaxation factor to cap the normal force calculated using the overlap of the daughter particles, so as to prevent the appearance of extremely high velocities of the fragments which would make simulations unrealistic [18]. In this study it is proposed that the contact overlaps between the progeny particles at the point of fragmentation are an artefact of fragments creation and should therefore be initialised to zero. A simple numerical approach is employed that eliminates all artificial overlaps at the moment of fragment creation, allowing only the real overlap which is the result of the external mechanical forces on the particles. In addition to the viscous damping with the coefficient of restitution for each collision, a global damping term has been introduced which applies opposing damping forces to each fragment to reduce any excessive acceleration that may result from the explicit algorithm involving very small particles. The global damping suppresses particle motion and should not be used without careful justification. In this paper, unless explicitly stated, global damping is set to zero and where it is used, its effect is shown clearly for scientific discussion.

3. Materials and methods

3.1. Materials and experiments

Three materials were selected for this study: a copper ore, a granulite and a limestone. They were selected for their different breakage responses, thus allowing to verify and validate the model for a wide

range of resistances to breakage, having already been used as the basis for other benchmarking studies on simulating breakage in DEM [12,23]. A summary of physical characteristics of the samples is given in Table 3, including the results from standard crushability and grindability tests [43] for reference only.

Parameters in the model equations described in section 2 have been fitted from single-particle impact-breakage experiments using impact load cell devices [26]. A summary of the model parameters is given in Table 4, where the data can be found in previous publications [44,45]. In the model verification using single particle breakage (section 4.1), the truncation ratio E_{max}/E_{50} was set to 4 to maintain consistency with the work presented in [23], whereas in the model validation using particle beds breakage (section 4.2), it was set to 100. This later value is consistent with nearly no upper truncation of the distribution, which was the case of the parameters listed in Table 4 [44,45].

Experimental data for validating the model were collected from impacts on unconfined monodispersed particle beds. They were obtained from the work of Barrios [46], having already been partially reported in previous publications [12,23,44]. Experiments were run in triplicate and the average values of the output, namely, mass of material passing the initial narrow size (broken mass), radius of capture and particle size

distribution, are herein reported. Particles tested were contained in the size range 6.3–4.75 mm. Bed arrangements used in the experiments included 1, 2, 3 and 4 rings of particles around a central particle in an approximately hexagonal packing (see Fig. 7a) – this is referred to as a monolayer arrangement. In addition, impacts on beds containing three and five layers of particles (see Fig. 7b) were also tested. In the case of the latter, a fragile paper ribbon was used to contain the particles from falling-off the bed prior to impact, while maintaining unconfined stressing conditions. An 88 mm diameter steel ball weighing 2.78 kg was used in all tests. The stressing (impact) energy was controlled by varying the drop height, resulting in impact velocities that varied from 1.0 to 2.5 m/s. Upon completion of the test the entire material was collected and subjected to size analysis by wet sieving.

In the experiments, a procedure was used to estimate the maximum radius in the bed of particles that were captured by the falling steel ball. It consisted of placing carbon paper and a white paper sheet underneath the bed and then using image analysis to analyse the area and radius of the impressions on the carbon paper [44]. This data has served as the basis for the development of an analytic model of particle capture in a monolayer bed in the authors´ laboratory, described elsewhere [44].

3.2. DEM simulations

DEM simulations were carried out using Altair EDEM [41], with the Hertz-Mindlin contact model. Table 5 presents the material parameters adopted in the simulations, where estimates of Young's modulus and Poisson's ratio were collected from the literature. Table 6 presents the contact parameters adopted in the simulations to validate the breakage model, which were estimated on the basis of data from the copper ore [12] but were used for all three materials. This assumption is valid for comparative purposes, although it is recognized that the calibration of contact parameters is an important step prior to any DEM simulation.

Simulations were conducted for both single impact and double impact modes. Single impact simulations were performed by propelling particles against a steel plate at different velocities to represent a wide range of stressing energies. Double impact tests were simulated through drop weight tests (DWT) [36] using a steel cylinder as striker. In this case, the stressing energy involved in the two different contacts (striker-particle and particle-anvil) were added (Eq. 14). Different impact energies were achieved by changing the drop height and the mass of the falling cylinder. A total of 250 virtual particles were stressed under each impact condition, from which the proportion broken was estimated, as well as the progeny size distribution.

Simulations were conducted to compare them to model predictions of breakage probability in single or multiple impacts and particle frag-
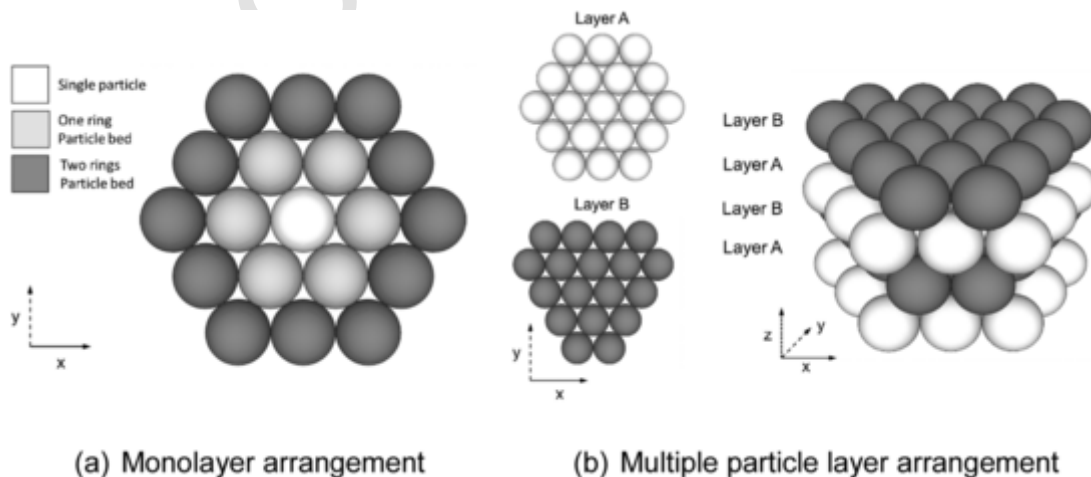
Table 3
Standard breakage characteristics of the samples.

Measure	Unit	Copper ore	Limestone	Granulite
Bond crushability work index	kWh/t	19.7	5.0	15.2
Bond ball mill work index	kWh/t	14.7	7.5	10.4
JKDWT A*b	% t/kWh	39.3	772	38.4

Table 4
Summary of particles breakage parameters adopted in the simulations.

Parameter	Copper ore	Limestone	Granulite
E_∞ (J/kg)	213.5	7.0	130.7
d_o (mm)	8.07	100	1.10
φ	1.22	0.80	1.99
σ	0.799	0.801	0.903
γ	5.0	5.4	5.4
A (%)	67.7	53.3	47.5
b'	0.029	0.033	0.027
$\alpha_{1.2}/\beta_{1.2}$	0.51/11.95	0.19/7.78	0.43/10.26
$\alpha_{1.5}/\beta_{1.5}$	1.07/13.87	0.56/7.51	0.92/10.74
α_2/β_2	1.01/8.09	0.78/5.55	1.31/9.15
α_4/β_4	1.08/3.03	1.12/3.01	1.18/2.97
α_{25}/β_{25}	1.01/0.53	1.17/0.54	0.93/0.49
α_{50}/β_{50}	1.03/0.36	1.43/0.40	0.92/0.39
α_{75}/β_{75}	1.03/0.30	1.92/0.42	0.90/0.31

(a) Monolayer arrangement   (b) Multiple particle layer arrangement

Fig. 7. Illustration of particle arrangements used in simulations of unconfined impacts on particle beds.

Table 5
Material parameters used in the DEM simulations.

Parameter	Copper ore	Limestone	Granulite	Steel
Specific gravity (kg/m³)	2930	2710	2790	7800
Young's modulus (GPa)	52	20	45	210
Poisson's ratio (−)	0.25	0.25	0.20	0.30

Table 6
Contact parameters used in the DEM simulations.

Parameter	Particle/Steel	Particle/Particle	Steel/Steel
Coefficient of static friction – Csf	0.50	0.49	0.50
Coefficient of rolling friction – Crf	0.01	0.27	0.01
Coefficient of restitution – Cr	0.39	0.48	0.50

mentation. Breakage probability in the simulations was assessed by recording the number of particles replaced. Breakage probability by multiple impacts and particle weakening by damage accrual was assessed in simulations of 20 repeated drops of 100 particles against a steel plate by counting the number of broken particles after each impact. A comparison with experimental data and a sensitivity analysis of the γ parameter (Eq. 6) was carried out to further verify the model.

In particle bed breakage simulations, particles of size 5.5 mm were placed in the geometrical configuration according to Fig. 7. Care was taken for each simulation to match the total mass of particle bed used in the same experimental configuration. Different bed configurations were used by incrementing the number of rings around a central particle (Fig. 7). Particles were evenly distributed based on the size of beds observed experimentally to ensure repeatability of capture radii of experiments. In order to mimic the paper ribbon used in experiments involving multiple bed layers, a cylindrical holding geometry was placed up to the instant of first contact of the dropping ball with the particles when it was immediately removed. Simulations were run in triplicate and the average results adopted.

The global minimum progeny size (d_{min}) in the simulations was set at 1/20th of the top particle size in the simulation, keeping in mind that each breakage event generates only particles down to about 1/5th of the parent size (Table 2). Another parameter required in the simulation is the minimum energy. It was introduced to prevent the software from wasting time in computations for contact energies that are too small for generating any damage, with the value 0.0001 J used in the present work. Time steps used in the simulations corresponded to 5% of the Rayleigh time in the breakage probability study, whereas in the fragmentation study a reduction to 2% of the Rayleigh time was necessary. Also, only the normal component of the stressing energy was considered in most simulations, so that c_s in Eq. (14) was set to zero. This selection is supported by evidence from a previous study on iron ore pellets [47]. An optimal value of the global damping parameter was selected by comparing size distributions predicted by the model and simulations. Finally, the parameter κ in Eq. (8) was set to 1.

4. Results and discussion

4.1. Model verification

4.1.1. Single-particle breakage probability

With the aim of demonstrating that the implementation in the API has captured properly the model capabilities, simulations were first compared to model predictions using the equations described in section 2. Firstly, the breakage probability described in detail in section 2.1 is verified. Fig. 8 compares the computed breakage probability from the simulations for both single impact and double impact (DWT) of particles of the different test materials to the model equations. Very good agreement was observed between simulations and the model for both modes of application of stresses to single particles. Predictions for sin-
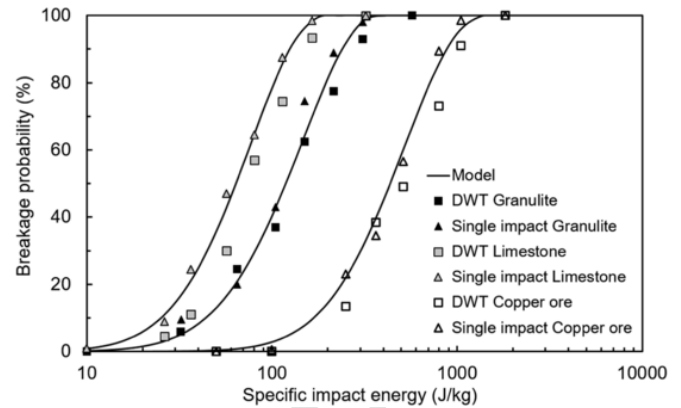

Fig. 8. Effect of specific impact energy and material on breakage probability of 5.5 mm particles for three materials for single and double impact against a steel surface. Lines represent the analytical model (section 2) and symbols represent simulations.

gle impact presented generally higher breakage probabilities than double impact (DWT), in spite of no discrimination of that in the model equations. This could be partially explained by the fact that minor mismatches may occur when summing the contributions of the stressing energy in the opposite poles (Eq. 14) of the particle for each time step in a DWT. Also evident in Fig. 8 is the ability of the model and simulation in discriminating the different materials in the size range studied.

The coefficient of restitution in a contact has been known to influence the results of a simulation using DEM [42]. With the aim of investigating the sensitivity of the proposed breakage model to the coefficient of restitution Cr adopted in the simulation, breakage probabilities are compared to simulation results for different Cr values for particle-steel contact. Results plotted in Fig. 9 show that the coefficient of restitution does not influence the breakage probability. This is due to the fact that during a stressing event, the available impact energy for breakage is the combination of the elastic and the dashpot energy. Furthermore, in the case where the particle does not break, its response after the impact will be influenced by the Cr, with a smaller bounce when a lower Cr is used and higher otherwise. Thus, the Cr is likely to have a greater influence in a dynamic system with multiple stressing events.

The effect of contact stiffness of the impact surface is also analysed in Fig. 9, which compares impacts of copper ore particles on a steel ($k_m = 230$ GPa) and a rubber surface ($k_m = 1.3$ GPa), as well as a sur-
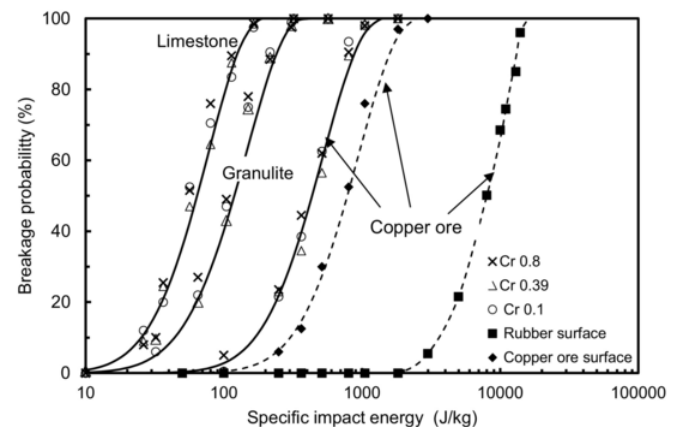

Fig. 9. Effect of specific impact energy and coefficient of restitution (Cr) on the breakage probability of 5.5 mm particles of the different materials for single impact against a steel target (solid lines). Results are also presented from impacts of copper ore particles with a coefficient of restitution of 0.39 against other surfaces (dashed lines). Lines represent the analytical model and symbols the simulations.

face with the same stiffness as the copper ore (k_m = 55.5 GPa). Both model and simulations were able to capture the reduction in breakage probability with the reduction in stiffness of the target surface, as more of the energy of the stressing event will be used in deforming the target (Eq. 4). This shows that the value of shear modulus of the material and the target surface used in the simulation should be selected carefully in a DEM simulation involving particle breakage, obeying the ratio given in Eq. (4). It is worth noting that if $E_k^{'}/m_p$ is plotted in the x-axis instead of E_k/m_p, results for copper ore for the three different surfaces in Fig. 9
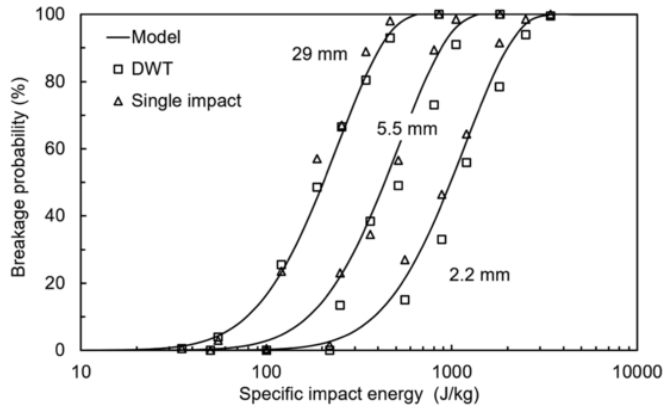
Fig. 10. Effect of specific impact energy and particle size on the breakage probability of copper ore. Lines represent the analytical model and symbols the simulation results for impacts involving steel surfaces.

Fig. 11. Comparison between predictions of proportion broken after repeated impacts of 37.5 mm copper ore particles at 94.7 J/kg against a steel target, showing the influence of varying the parameter γ.

would superimpose, since E_k is the stressing energy and $E_k^{'}$ is the fraction that is available for breakage of the particle.

Equations in section 2.1 demonstrate that the model response is typically influenced by particle size within the size range of interest. This is illustrated in Fig. 10, which shows that both the model and simulation results are able to account for the reduction in breakage probability as particle size reduces.

Sensitivity of the simulations to time step was also analysed and it was found that breakage probability did not change for time steps equal or smaller than 5% of Rayleigh time. Results are, however, omitted for brevity.

After individual impacts such as those simulated in Figs. 8-10, in the event that a particle does not break, then the model (Eqns. 5 and 6) predicts that the specific energy required for breakage reduces, making it more amenable to break in another stressing event. In order to verify the model implementation, simulations with repeated impacts are compared to model predictions in Fig. 11. It shows that simulations matched the predictions using the model for the different values of the damage accumulation coefficient γ, which characterizes the amenability of the material to sustain damage and yet not break.

4.1.2. Single-particle fragment size distribution

An important verification of the model implementation relates to the fragment size distribution. In this case it is important to highlight that the DEM simulation captures the sequence of primary breakage events that occur in the single particle impact test. This is illustrated in Fig. 12, which shows snapshots of the simulations in which particles are impacted at different specific stressing energies and a succession of breakage events occur. It shows that at a lower stressing energy a single breakage event occurs, whereas at a higher stressing energy, successive replacements occur, resulting in a finer fragment size distribution. It is also worth noticing that the first (primary) breakage event in both cases results in similar distributions of progeny fragments. The substantial overlaps of the progeny fragments are also evident, which, as explained earlier, is an artefact of fragments creation and are initialised to zero so that only the contact overlaps arising from the resultant forces on the fragments are used in the computations. This approach provides a robust calculation of the dynamic interaction between these fragments.

In order to demonstrate the validity of the proposed approach Fig. 13 compares the size distributions predicted by the model (Eqns. 7 and 10) to those computed considering the sizes of spheres as they appear in the DEM simulations without replacing the ´dummy` and resolved unbreakable particles by the fines they represent. It shows that the simulation results with low to intermediate stressing energies are in good agreement with the model for the coarse sizes. It also shows that, although simulations extend down to the global minimum size of 1.45 mm, which is 1/20th of the initial particle size in question, the computed results for sizes below 6 mm (about 1/5th of the parent particle size) severely underestimated the model predictions. At the lowest
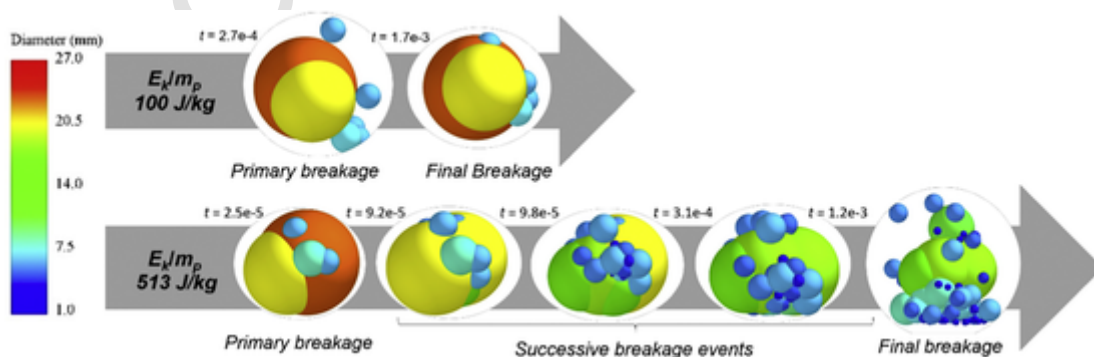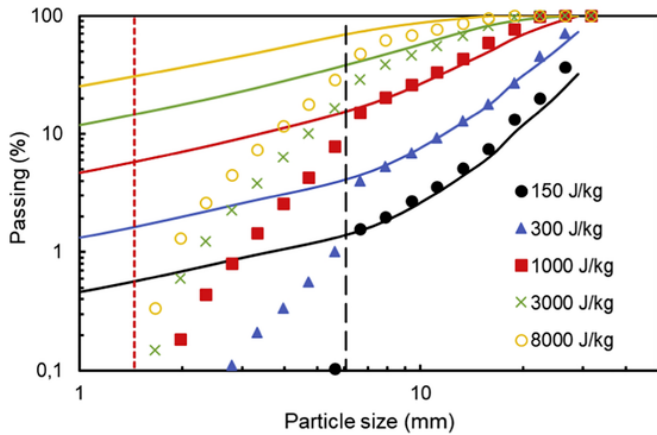

Fig. 12. Snapshots of outcomes of simulations of impacts of 29 mm copper ore particles against a steel target, showing the successive breakage events (top: impact at low E_k/m_p with no successive breakage; bottom: impact at high E_k/m_p with successive breakage).

Fig. 13. Comparison of modelled (lines) and simulated (symbols) size distributions from impact of 29 mm copper ore particles against a steel target at different specific stressing energies in which simulated distributions were computed considering the sphere sizes that appear in the DEM simulations. Dashed black line represents the minimum fragment size considering the families (Table 2) and red dashed line represents the minimum global fragment size.

specific stressing energy of 150 J/kg, a significant fraction of the particles remains unbroken, and this is properly taken into account both in simulations and in model predictions.

The results using the full procedure proposed in the present work are presented in Fig. 14, in which the fines represented by the ´dummy` particles (Eq. 9) as well as those associated to the unbreakable resolved particles (Eq. 11) are included to represent each size distribution. It shows that in this case very good agreement between simulation and the model down to sizes below 1 mm is reached. It also shows that nearly no discontinuity appears in the computed size distributions either below the minimum replacement size, depicted by the black vertical line in Fig. 14, or the global minimum size (d_{min}), represented by the red line. However, the results show that the simulations underestimate the size distributions given by the model at high stressing energies. This may be partially explained by the fact that ´dummy` particles are not allowed to further break and only the first breakage event is considered in the case of the unbreakable resolved particles, whereas in high-energy impacts against a target both would likely undergo additional breakage events. Another plausible explanation is related to the assumption of the value of κ in Eq. (8) which was assumed to be equal to one, whereas
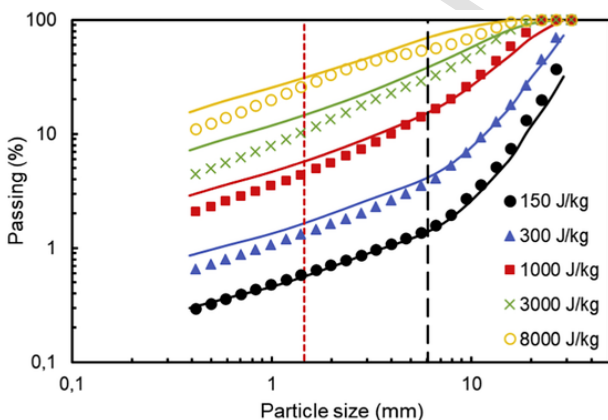

Fig. 14. Comparison of modelled (lines) and simulated (symbols) size distributions from impact of 29 mm copper ore particles against a steel target at different specific stressing energies considering both the resolved and unresolved particles. The black dashed line depicts the minimum fragment size considering the families (Table 2) and the red dashed line represents the minimum global fragment size.

at high stressing energies it may be as high as 1.38 for the copper ore [24]. Further, only the normal component is considered in the simulations ($c_s = 0$ in Eq. 14), whereas as soon as fragments are created a shear component appears between their interactions, which is not accounted for. The outcome is that the simulation approach introduces points of inflexion in the size distributions at specific stressing energies above 1000 J/kg that were neither contained in the model nor the experiments, as a result of the limitations listed above. It should also be noted that the good agreement observed in Fig. 14 was obtained by setting the global damping parameter to 0.3, which was used as default in the simulations reported in the present work for copper ore, unless stated otherwise.

Comparisons presented between model and simulations for the case of the drop weight test (Fig. 15) show the same general trend, although with a greater deviation between model predictions and simulations at high stressing energies for the reasons listed above. Good agreement was also observed for the other materials, but results are omitted for brevity.

The effect of stressing energy is analysed in greater detail in Fig. 16, in which the proportion passing 1/10th of the initial size of broken particles (t_{10}) is plotted for different materials for 29 mm particles. It shows the combined influence of particle fracture energies of the different materials as well as their different fragmentation patterns. Fig. 16
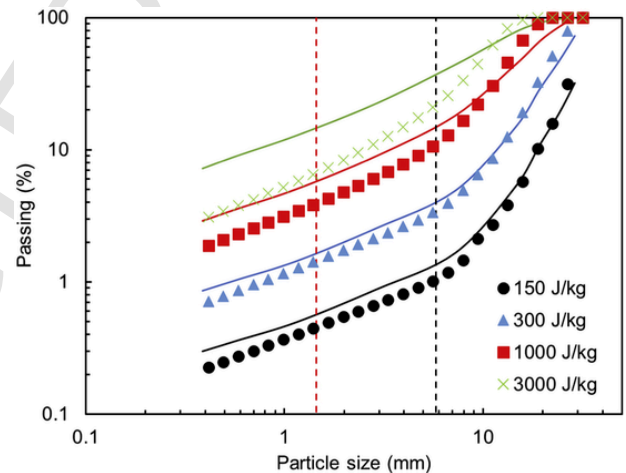

Fig. 15. Comparison of modelled and simulated size distributions from impact of 29 mm copper ore particles in a DWT at different impact energies considering both the resolved and unresolved particles. The black dashed line depicts the minimum fragment size considering the families (Table 2) and the red dashed line represents the minimum global fragment size.
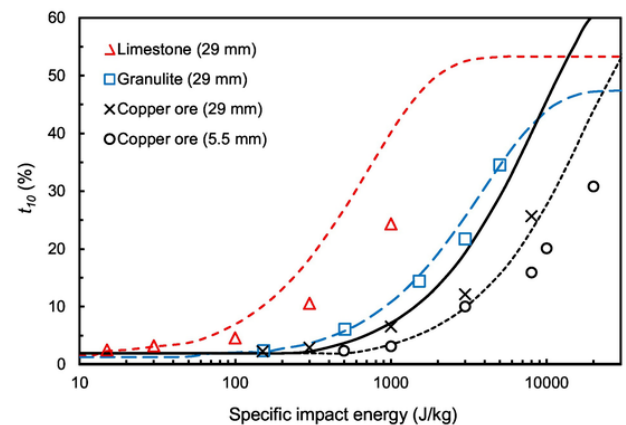

Fig. 16. Comparison between the modelled (lines) and simulated (symbols) t_{10} values for drop weight tests (DWT) of 29 mm particles of the different materials, including data for 5.5 mm copper ore particles.

also shows that the implemented model is able to provide simulation results which are in very good agreement with the model, in particular at low to intermediate t_{10} values. As already observed in Figs. 14 and 15, deviations increase in the case of higher stressing energies and greater intensities of fragmentation, in particular for limestone and copper ore. Included also in the figure are results for finer (5.5 mm) copper ore particles, which demonstrate the reduction in breakage intensity captured in both the model and the simulations as particle size reduces.

In DEM simulations, it is always worthwhile verifying if the computational time step selected allows achieving reliable numerical accuracy in the simulation. In addition, the use of global damping and the parameter c_s as described previously should also be checked. The sensitivity of these three parameters in the simulations for low and high stressing energies are presented in Figs. 17 to 19. Fig. 17 shows the effect of varying the time step for single stressing of copper ore particles, demonstrating that it can have a significant effect on the simulated size distribution. In the case of the lower stressing energy, simulation results nearly superimpose up to 4% of Rayleigh time step, demonstrating lower sensitivity to this parameter. However, at the higher stressing energy level, differences are observed in the predictions even down to 3% of Rayleigh time step, with convergence occurring only at 1–2% of Rayleigh time step. This significant effect at high stressing energies is
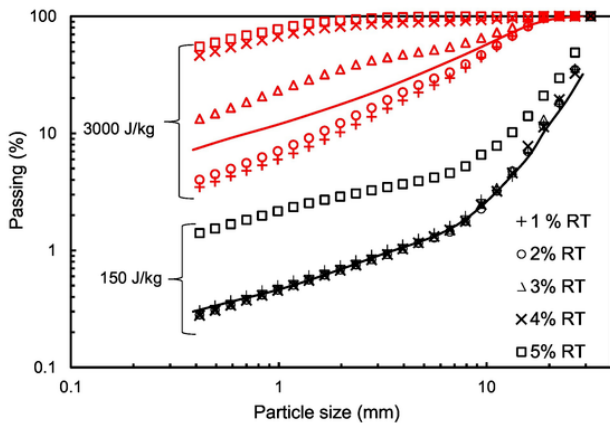

Fig. 17. Comparison of modelled and simulated size distributions from single impact of 29 mm copper ore particles against a steel target with global damping parameter equal to 0.3 and different time steps, represented as percent of Rayleigh time (RT). Solid lines represent the model and symbols the simulation results.
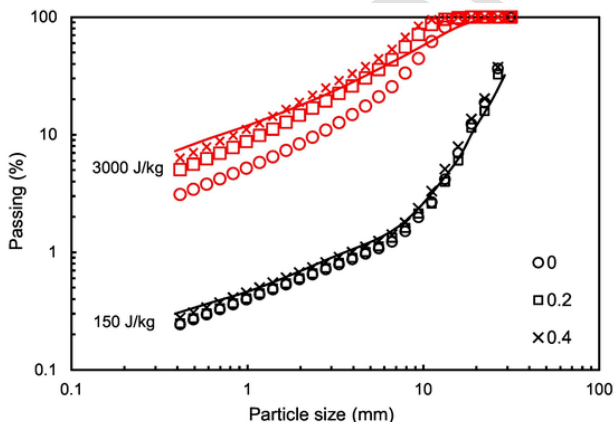

Fig. 18. Comparison of modelled and simulated size distributions from single impact of 29 mm copper ore particles in a DWT with different values of c_s, representing different contributions of the shear component in breakage (Eq. 14). Time step constant at 1% of RT and global damping parameter equal to 0. Solid lines represent the model and symbols the simulation results.
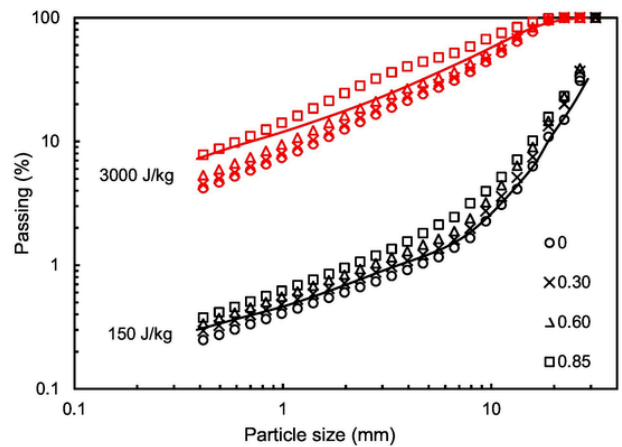

Fig. 19. Comparison of modelled and simulated size distributions from single impact of 29 mm copper ore particles against a steel target at two specific impact energies and with different values of global damping parameter. Time step constant at 1% of RT. Solid lines represent the model and symbols the simulation results.

likely associated to the high velocity of the particle in the particular case (>75 m/s) since the magnitude of deformation and the associated computed stressing energy increases significantly from one time step to the next, so that it may be lower than the fracture energy in one step and significantly larger than it in the following. The result is that the final value of t_{10}' in Eq. (8) may be higher.

The effect of the shear component in the simulations (c_s in Eq. 14) in shown in Fig. 18 for the case of DWT of copper ore, the case in which the larger deviations were found (Fig. 15). It shows that it had no effect on the predictions at the low specific stressing energy. This is not surprising, since the size distribution is essentially result of primary breakage, which occurred due to normal impact of the striker. At the higher energy, however, the increase in c_s resulted in significant increase in fineness and better agreement between simulations and the model. This may be explained by the fact that, even though the steel striker applied a normal impact to the parent particle, as soon as the first generation of progeny fragments is created, shear in addition to the normal component appears in the interactions among fragments and between fragments and the striker/anvil. As such, even accounting for a minor part of the shear component led to improved agreement. However, in spite of the apparently beneficial role of c_s, it is maintained at 0 for the remainder of the work, given evidence, presented elsewhere [47], that only the normal component contributes to breakage probability. Nevertheless, these simulation results, as well as the controversy that still exist in the literature regarding the importance of shear in breakage [47–49], demonstrate this topic requires further investigation.

The effect of the global damping parameter is shown in Fig. 19. Although relatively small compared to the effect of timestep, increasing the global damping parameter results in a finer size distribution, due to the fact that newly created fragments separate more slowly after creation, hence being more readily available for undergoing further breakage. In the present work, the value was maintained equal to zero for the materials, except for copper ore, which was set to 0.3.

4.2. Model validation

In this section, the predictive capability of the proposed breakage model is compared to results from impact experiments conducted on unconfined beds of particles. These include impact experiments on monolayer particle beds (three rings around a central particle as shown in Fig. 7) where the extent of the drop ball weight impact on the particle bed was estimated from measurements using carbon paper [12,46]. The DEM simulation predictions are compared to the experimental

measurements in Fig. 20 for copper ore, which shows that as the stressing energy increases, more material is ´captured` in the bed. This is explained by the fact that the drop ball is able to move further downwards with higher stressing energies, increasing the number of particles that are stressed in the monolayer bed. The resulting size distributions from these tests are compared in Fig. 21. It shows the very good agreement between simulations and experiments, thus demonstrating the validity of the simulation approach. It shows that the simulations captured the effect of not only more particles breaking with the increase in stressing energy, but also their breakage into finer fragments, giving rise to the increase in fineness of the fragment size distribution.

The effect of bed configuration on the broken mass in the bed is shown in Fig. 22 for the three materials studied. It shows that simulations were able to capture reasonably well the general trend observed in the experiments. More so, in the case of copper ore the simulations were able to describe the reduction in the amount of broken material resulting from the impact on beds with multiple particle layers. This is attributed to the combination of high resistance to breakage of copper ore and the loss of momentum in the dropping ball while penetrating the various layers. In the case of limestone, the simulations match the experiments for all monolayer cases but do not produce a good match to the experimental results for the multi-layer beds. The mismatch can be attributed to the fact that the contact parameters used in all the simulations were estimated only for the copper ore [12] but were applied to all other materials. Therefore, to assess the sensitivity against the selected contact parameters, the coefficient of rolling friction (Crf) for the steel-particle contact was modified from the value of 0.01 (Table 6) to
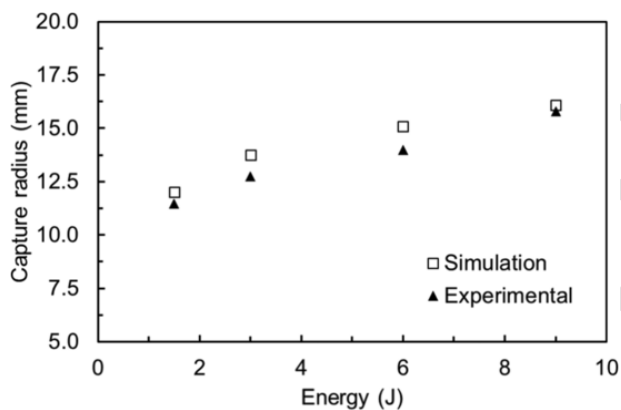

Fig. 20. Comparison of the capture radius as a function of impact energy in experiments and simulations of impact with an 88–mm diameter ball in a monolayer bed of 4.75–6.3 mm copper ore particles.
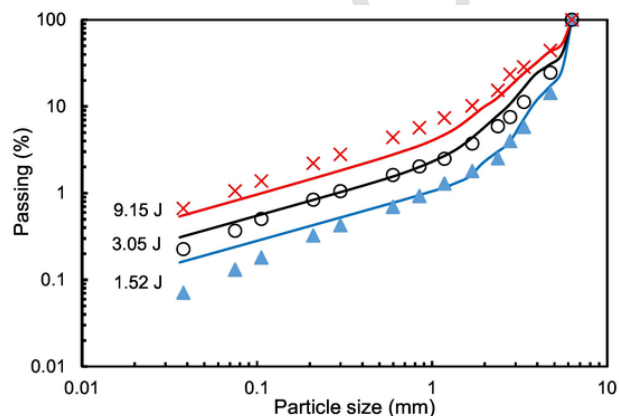

Fig. 21. Comparison of the size distributions in experiments and simulations from impact of an 88 mm diameter ball in a monolayer bed of 4.75–6.3 mm copper ore particles at different impact energies.

0.33 and simulations for limestone and granulite were repeated. These results (Fig. 22) show that such change results in improved agreement between the simulations and the experiments for limestone and has no significant effect on granulite. Increasing the Crf highlights the difficulty of particles to be pushed further away by the drop weight. The greater the interlocking the higher the stresses, so that a larger number of particles of the more brittle material (limestone) can break, whereas the increase is only marginal for the tougher material (granulite).

The effect of bed configuration on the size distribution of the material after impact is then analysed in Fig. 23 for copper ore and granulite on the basis of contact parameters from Table 6. The results show that the simulations can predict well the material-dependent responses of the different bed configurations of the particles subject to impact at a fixed stressing energy E_k. The good fidelity of the model to predict the size distributions down to 0.1 mm, which is equivalent to about 1/50th of the initial size, attests to the ability of the procedure proposed in the present work to predict breakage.

4.3. Discussion

In the present work the breakage model represented by Eqns. (1) to (16) has been implemented, as an API, in the software EDEM using spheres. The same model has been previously implemented in the software Rocky DEM [23] using polyhedral particles. A comparison between the two shows that both captured equally well the material and stressing energy-dependent breakage probability, both for single (Figs. 8-10) and multiple impacts (Fig. 11). The key differences appear in their description of the progeny size distribution. The particle replacement using polyhedral particles does not require superposition of the fragments and uses Voronoi tessellation to create the fragments. The spherical particle replacement includes superposition of fragments and uses a novel method to handle the artificial overlaps and prevent ´explosive` ejection of fragments. Furthermore, the present work includes a new approach that describes the unresolved fines, whereas the implementation in Rocky DEM 4.2 did not [23]. The particle replacement scheme in the present work provided greater control of the fragment size distribution than that achieved using the Voronoi tessellation scheme used for polyhedral particles [23]. Finally, since different machine configurations were used in the two studies, a comparison of computational effort was not feasible. However, an earlier study [12] demonstrated the reduced effort involved with particle replacement with spheres compared to polyhedral particles.

The particle replacement approach implemented overcame several of the known limitations in the literature concerning sphere-based replacement [12], while maintaining their computational efficiency.

5. Conclusions

A detailed model describing body breakage of brittle particulate materials has been implemented in EDEM. The breakage model incorporates material- and size-dependent variability in particle fracture energies, material weakening by unsuccessful stressing events and a stochastic particle replacement approach informed by extensive experimental data on impact testing. It further includes an extension below the minimum size used in the simulation to describe the unresolved fines and achieves a conservation of mass in the system.

The breakage model has been verified in great detail by comparison of model predictions to simulations of single-particle breakage, which demonstrated that the effects in variability in particle fracture energies, particle size, material and impact surface have been properly described. The results showed that the model was able to predict fragment size distributions very accurately, with satisfactory predictions extending beyond the minimum fragment size used in the DEM simulation. The approach has achieved a strict control of fragment size distribution, with
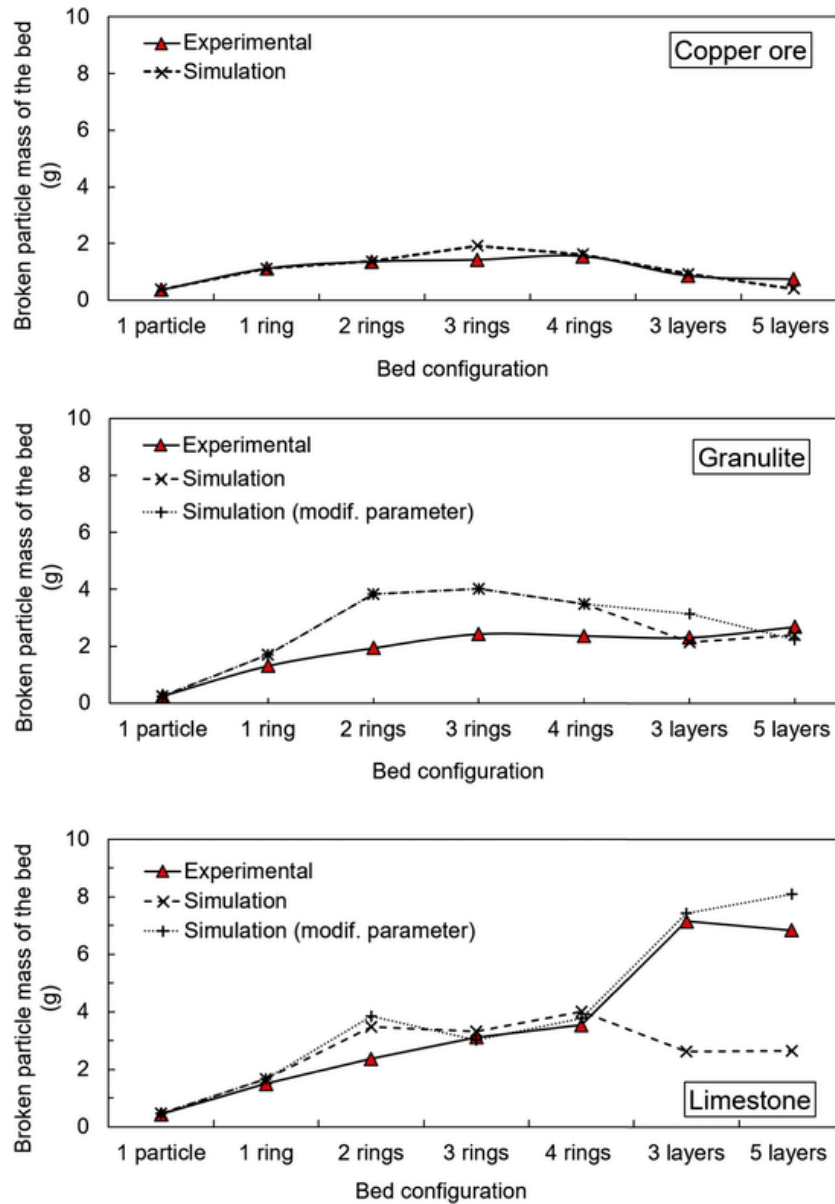
Fig. 22. Comparison of experimental and simulated values of broken mass in different bed configurations for a single impact at 3.05 J from an 88 mm diameter ball. Additional simulations for granulite and limestone conducted using steel-particle Crf (modif. parameter) of 0.33.

deviations between simulations and the model only appearing at high stressing energies.

Model validation has been carried out by comparing the simulations with the experimental data from breakage of particles in unconfined particle beds in monolayer and multilayer configurations. It showed that the model was able to predict accurately the radius of capture and the broken mass from impacts at different energies and bed configurations, as well as the size of the resulting debris.

CRediT authorship contribution statement

Luís Marcelo Tavares: Conceptualization, Methodology, Resources, Writing – original draft, Writing – review & editing, Supervision, Project administration, Funding acquisition. **Victor A. Rodriguez:** Methodology, Software, Validation, Formal analysis, Investigation, Data curation, Writing – original draft, Writing – review & editing, Visualization. **Marina Sousani:** Conceptualization, Validation, Formal analysis, Resources, Writing – original draft, Writing – review & editing, Project administration. **Carles Bosch Padros:** Soft-

ware, Validation, Formal analysis. **Jin Y. Ooi:** Conceptualization, Formal analysis, Writing – original draft, Writing – review & editing.

Declaration of Competing Interest

The authors declare that they have no known competing financial interests or personal relationships that could have appeared to influence the work reported in this paper.
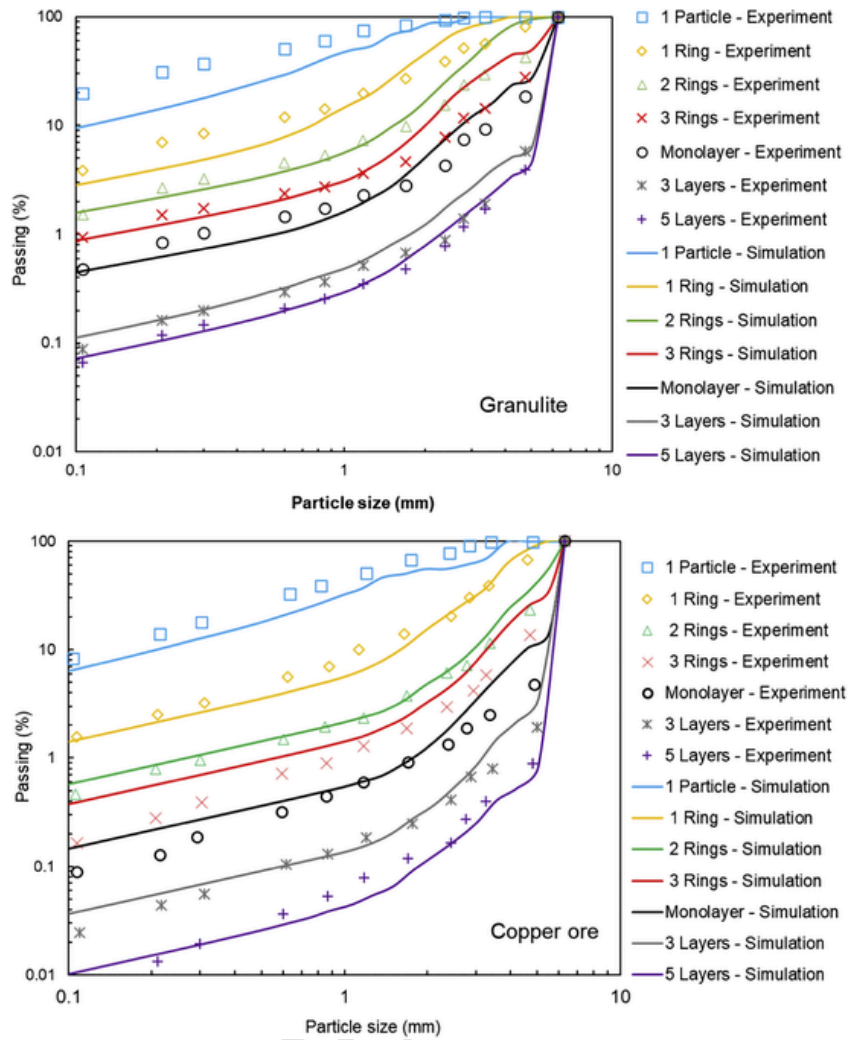
Fig. 23. Comparison between size distributions of the bed material after impact at 3.05 J with an 88-mm diameter steel ball for copper ore (top) and granulite (bottom). Symbols represent experimental data and lines simulations.

Appendix A. Derivation of elastic energy partition equation (Eq. 4)

Consider the contact of spheres whose curvatures are approximated by parabolas. The contact surface is given by a disc of radius a. From the potential theory [50,51] the pressure distribution in the surface of contact is given by

$$p(r) = \frac{K_e}{\pi} \left(-\frac{\alpha}{\sqrt{a^2 - r^2}} + \frac{r^2}{K_e \sqrt{a^2 - r^2}} - \frac{\sqrt{a^2 - r^2}}{K_g} \right)$$

(A.1)

where α represents the approach between two points distant from the contact and r is the distance from the center of the disc. K_g and K_e are given by

$$K_g = \frac{R_{c1} R_{c2}}{R_{c1} + R_{c2}}$$

(A.2)

and

$$K_e = \frac{k_1 k_2}{k_1 + k_2}$$

(A.3)

where R_{c1} and R_{c2} are the radii of curvature. k is called the stiffness of each particle and is given by.

$$k_1 = \frac{Y_1}{1 - \mu_1^2} \text{ and } k_2 = \frac{Y_2}{1 - \mu_2^2}. \tag{A.4}$$

where Y and μ are the modulus of elasticity and the Poisson's ratios of the contacting particles, respectively.

Eq. (A.1) represents the most general form of a physically acceptable direct traction distribution which produces contact over a finite disk [52]. If, however, the possibility of cohesive tension is excluded, it is essential that the pressure falls continuously to zero at the rim of the contact, i.e. p $(a) = 0$. This immediately gives

$$\alpha = \frac{a^2}{K_g} \tag{A.5}$$

Eq. (A.1) then becomes

$$p(r) = -\frac{2K_e}{\pi K_g} \sqrt{a^2 - r^2} \tag{A.6}$$

The radius of the contact a can be found by ensuring vertical equilibrium such that

$$F = -\int_0^a 2\pi r p(r) \, dr \tag{A.7}$$

where F is the vertically applied load. Substituting Eq. (A.6) in Eq. (A.7) it gives

$$F = \frac{4a^3 K_e}{3K_g} \tag{A.8}$$

Now substituting Eq. (A.5) in Eq. (A.7) it gives

$$F = \frac{4}{3} K_e K_g^{1/2} \alpha^{3/2} \tag{A.9}$$

This is the general constitutive equation describing one-point contact of curved surfaces. This equation is only valid for quasi-static conditions, i.e., when the impact time is longer than the time taken for the elastic strain wave to travel within the solid. Eq. (A.6) can be written as

$$p(r) = -p_o \sqrt{1 - (r/a)^2} \tag{A.10}$$

where

$$p_o = \frac{1}{\pi} \left[6F \left(\frac{K_e}{K_g} \right)^2 \right]^{1/3} \tag{A.11}$$

Substituting Eq. (A.5) in (A.8), equating to (A.11) and rearranging it gives

$$\alpha = \frac{\pi a p_o}{2K_e} \tag{A.12}$$

Substituting Eq. (A.3) in (A.11) it gives

$$\alpha = \frac{\pi a p_o}{2k_1} + \frac{\pi a p_o}{2k_2} \tag{A.13}$$

which shows that the deformation in each of the bodies is given by $\Delta_i = \pi a p_o/(2k_i)$. The ratio of the deformations in each of the bodies is given by

$$\frac{\Delta_1}{\Delta_2} = \frac{k_2}{k_1} \tag{A.14}$$

Given that the overall deformation of the system is given by $\alpha = \Delta_1 + \Delta_2$, Eq. (A.14) can be written as

$$\Delta_1 = \alpha \left(\frac{k_2}{k_1 + k_2} \right) \tag{A.15}$$

and

$$\Delta_2 = \alpha \left(\frac{k_1}{k_1 + k_2} \right) \tag{A.16}$$

Eqs. (A.15) and (A.16) allow estimation of the individual deformations in each of the spheres in contact, given a measurement of the approach α and the stiffness of the bodies in contact.

The constitutive equation of the contact is given by Eq. (A.9). It does not, however, discriminate between the relative indentations in each of the particles. The constitutive equations of each of the particles can be expressed by

$$F_1 = \frac{4}{3} K_1^* K_g^{1/2} \Delta_1^2 \tag{A.17}$$

and

$$F_2 = \frac{4}{3} K_2^* K_g^{1/2} \Delta_2^2 \tag{A.18}$$

The constants K_1^* and K_2^* must now be determined. Assuming force continuity at the surface of contact, the loads experienced by each surface in contact are equal ($F_1 = F_2 = F$) so that Eqns. (A.17) and (A.18) and substituting Eq. (A.13) gives

$$\frac{K_1^*}{K_2^*} = \left(\frac{k_1}{k_2}\right)^{3/2} \tag{A.19}$$

Manipulating algebraically Eqns. (A.9) and (A.19), and as $\alpha = \Delta_1 + \Delta_2$ it gives

$$K_1^* = k_1 \left(\frac{k_1 + k_2}{k_2}\right)^{1/2} \tag{A.20}$$

Now substituting Eq. (A.20) in Eq. (A.16) we obtain the constitutive equations of each particle, given by

$$F = \frac{4}{3} k_1 \left(\frac{k_1 + k_2}{k_2}\right)^{1/2} K_g^{1/2} \Delta_1^{3/2} \tag{A.21}$$

$$F = \frac{4}{3} k_2 \left(\frac{k_1 + k_2}{k_1}\right)^{1/2} K_g^{1/2} \Delta_2^{3/2} \tag{A.22}$$

The elastic energy stored in the contact in the collision between two particles is given by

$$E = \frac{8}{15} k_1 \left(\frac{k_1 + k_2}{k_2}\right)^{1/2} K_g^{1/2} \Delta_1^{3/2} \tag{A.23}$$

Using Eq. (A.23) the elastic energy stored in each particle can be calculated by

$$E_1 = \frac{8}{15} K_g^{1/2} k_1 \left(\frac{k_1 + k_2}{k_2}\right)^{1/2} \Delta_1^{5/2} \tag{A.24}$$

$$E_2 = \frac{8}{15} K_g^{1/2} k_2 \left(\frac{k_1 + k_2}{k_1}\right)^{1/2} \Delta_2^{5/2} \tag{A.25}$$

The ratio between the elastic energies stored in each of the particles is

$$\frac{E_1}{E_2} = \left(\frac{k_1}{k_2}\right)^{3/2} \left(\frac{\Delta_1}{\Delta_2}\right)^{5/2} \tag{A.26}$$

Substituting Eq. (A.14) in (A.26) and rearranging it finally gives the ratio of the elastic energy that is stored in particle #1 results in the expression for e

$$\frac{E_1}{E_1 + E_2} = \frac{k_2}{k_1 + k_2} \tag{A.27}$$

The derivation assumes a perfectly elastic contact between the particles, which is valid under very particular conditions. It also considers only quasi-static collisions, that is, with no wave propagation effects. Under these conditions it yields that the energy partition (Eq. A.27) is independent of radius of curvature, that is, of size of particles involved in the collision, which may be assumed to be a valid approximation. The validity of Eq. (A.27) to describe energy partition in collisions with mismatched particle masses and velocities and under conditions that differ from those assumed in the model is yet to be demonstrated.

References

[1] A. Datta, R.K. Rajamani, A direct approach of modeling batch grinding in ball mills using population balance principles and impact energy distribution, Int. J. Miner. Process. 64 (2002) 181–200.

[2] S. Beinert, G. Fragnière, C. Schilde, A. Kwade, Multiscale simulation of fine grinding and dispersing processes: stressing probability, stressing energy and resultant breakage rate, Adv. Powder Technol. 29 (2018) 573–583.

[3] X. Chen, L.G. Wang, J.Y. Ooi, A DEM-PBM multiscale coupling approach for the prediction of an impact pin mill, Powder Technol. 366 (2020) 408–419.

[4] A.L.R. Oliveira, V.A. Rodriguez, R.M. de Carvalho, M.S. Powell, L.M. Tavares, Mechanistic modeling and simulation of a batch vertical stirred mill, Miner. Eng. 156 (2020) 106487.

[5] D.O. Potyondy, P.A. Cundall, A bonded-particle model for rock, Int. J. Rock Mech. Min. Sc. 41 (2004) 1329–1364.

[6] N. Brown, J.Y. Ooi, J.F. Chen, A bond model for DEM simulation of cementitious materials and deformable structures, Granul. Matter 16 (2014) 299–311.

[7] A.V. Potapov, C.S. Campbell, Computer simulation of impact-induced particle breakage, Powder Technol. 81 (1994) 207–216.

[8] A.V. Potapov, C.S. Campbell, Parametric dependence of particle breakage mechanisms, Powder Technol. 120 (2001) 164–174.

[9] D. Wei, B. Zhao, D.D. da Costa, Y. Gan, An FDEM study of particle breakage under

rotational point loading, Eng. Fract. Mech. 212 (2019) 221–237.

[10] L. Guang-Yu, X. Wen-Jie, N. Govender, D.N. Wilke, A cohesive fracture model for discrete element method based on polyhedral blocks, Powder Technol. 359 (2020) 190–204.

[11] L.F. Orozco, J.-Y. Delenne, P. Sornay, F. Radjai, Discrete-element model for dynamic fracture of a single particle, Int. J. Solids Struct. 166 (2019) 47–56.

[12] N. Jiménez-Herrera, G.K.P. Barrios, L.M. Tavares, Comparison of breakage models in DEM in simulating impact on particle beds, Adv. Powder Technol. 29 (2018) 692–706.

[13] J.A. Åström, H.J. Herrmann, Fragmentation of grains in a two-dimensional packing, Eur. Phys. J. B. 5 (1998) 551–554.

[14] P.W. Cleary, Recent advances in DEM modelling of tumbling mills, Miner. Eng. 14 (2001) 1295–1319.

[15] H. Li, G. McDowell, I. Lowndes, Discrete element modelling of a rock cone crusher, Powder Technol. 263 (2014) 151–158.

[16] P.W. Cleary, M.D. Sinnott, Simulation of particle flows and breakage in crushers using DEM: part 1 – compression crushers, Miner. Eng. 74 (2015) 178–197.

[17] J.P. De Bono, G.R. McDowell, The fractal micro mechanics of normal compression, Comput. Geotech. 78 (2016) 11–24.

[18] G.K.P. Barrios, N. Jiménez-Herrera, L.M. Tavares, Simulation of particle bed breakage by slow compression and impact using a DEM particle replacement model, Adv. Powder Technol. 31 (2020) 2749–2758.

[19] W. Zhou, D. Wang, G. Ma, X. Cao, C. Hu, W. Wu, Discrete element modeling of particle breakage considering different fragment replacement modes, Powder Technol. 360 (2020) 312–323.

[20] G.W. Delaney, R.D. Morrison, M.D. Sinnott, S. Cummins, P.W. Cleary, DEM modelling of non-spherical particle breakage and flow in an industrial scale cone crusher, Miner. Eng. 74 (2015) 112–122.

[21] A.V. Potapov, J.A. Herbst, M. Song, A DEM-PBM fast breakage model for simulation of comminution processes, Proc. Discrete Element Methods, Brisbane, August, 2007.

[22] J. Lichter, K. Lim, A. Potapov, D. Kaja, New developments in cone crusher performance optimization, Miner. Eng. 22 (2009) 613–617.

[23] L.M. Tavares, F.P. André, A. Potapov, C. Maliska Jr., Adapting a breakage model to discrete elements using polyhedral particles, Powder Technol. 362 (2020) 208–220.

[24] L.M. Tavares, A.S. das Chagas, A stochastic particle replacement strategy for simulating breakage in DEM, Powder Technol. 377 (2021) 222–232.

[25] S. Yashima, Y. Kanda, S. Sano, Relationships between particle size and fracture energy or impact velocity required to fracture as estimated from single particle crushing, Powder Technol. 51 (1987) 277–282.

[26] L.M. Tavares, Breakage of single particles: Quasi-static, in: A.D. Salman, M. Ghadiri, M.J. Hounslow (Eds.), Handbook of Particle Breakage, 12, Elsevier, 2007, pp. 3–68.

[27] L.M. Tavares, R.P. King, Modeling of particle fracture by repeated impacts using continuum damage mechanics, Powder Technol. 123 (2002) 138–146.

[28] H. Schubert, On the microprocesses of comminution, Aufber.–Techn. 5 (1987) 237–246.

[29] L.M. Tavares, P.B. Neves, Microstructure of quarry rocks and relationships to particle breakage and crushing, Int. J. Miner. Process. 87 (2008) 28–41.

[30] M. Becker, A. Kwade, J. Schwedes, Stress intensity in stirred media mills and its effect on specific energy requirement, Int. J. Miner. Process. 61 (2001) 189–208.

[31] L.M. Tavares, R.M. de Carvalho, Modeling ore degradation during handling using continuum damage mechanics, Int. J. Miner. Process. 101 (2011) 21–27.

[32] L.M. Kachanov, Time of the rupture process under creep conditions (in Russian), Izv. Akad. Nauk AN SSSR 8 (1958) 26–31.

[33] L.M. Tavares, Analysis of particle fracture by repeated loading as damage accumulation, Powder Technol. 190 (2009) 327–339.

[34] E. Çinlair, Probability and Stochastics, Springer, 2010.

[35] P.P. Cavalcanti, R.M. de Carvalho, A.S. das Chagas, M.W. da Silveira, L.M. Tavares, Surface breakage of fired iron ore pellets by impact, Powder Technol. 342 (2019) 735–743.

[36] T.J. Napier-Munn, S. Morrell, R.D. Morrison, T. Kojovic, Mineral Comminution Circuits: Their Operation and Optimization, JKMRC Monograph Series in Mining and Mineral Processing, Brisbane, 1996.

[37] F. Saeidi, L.M. Tavares, M. Yahyaei, M. Powell, A phenomenological model of single particle breakage as a multi-stage process, Miner. Eng. 98 (2016) 90–100.

[38] L.M. Tavares, Role of particle microstructure in comminution, Proc. 19th Int. Min. Proc. Congr., Rome, vol. C, 2000 C4–99 to C4–106.

[39] R.M. de Carvalho, A. Secchi, L.M. Tavares, A new energy-based breakage function model and optimization procedure for mechanistic comminution models, 14th European Symposium on Comminution and Classification, 2015, pp. 1–4 Gothenburg.

[40] R.P. King, Modeling and Simulation of Mineral Processing Systems, Butterworth-Heinemann, 2001.

[41] EDEM, User Guide, DEM Solutions, Edinburgh, UK, 2020.

[42] N.S. Weerasekara, M.S. Powell, P.W. Cleary, L.M. Tavares, M. Evertsson, R.D. Morrison, J. Quist, R.M. Carvalho, The contribution of DEM to the science of comminution, Powder Technol. 248 (2013) 3–24.

[43] A. Mwanga, J. Rosenkranz, P. Lamberg, Testing of ore comminution behavior in the geometallurgical context—a review, Minerals 5 (2015) 276–297.

[44] G.K.P. Barrios, R.M. de Carvalho, L.M. Tavares, Modeling breakage of monodispersed particles in unconfined beds, Miner. Eng. 24 (2011) 308–318.

[45] R.M. de Carvalho, L.M. Tavares, Predicting the effect of operating and design variables on breakage rates using the mechanistic ball mill model, Miner. Eng. 43 (2013) 91–101.

[46] G.K.P. Barrios, Estudo da quebra de leitos de partículas visando a aplicação na modelagem generalizada da cominuição, M.Sc. thesis, Universidade Federal do Rio de Janeiro, Rio de Janeiro, 2010.

[47] P.P. Cavalcanti, H.A. Petit, A.D. Thomazini, R.M. de Carvalho, L.M. Tavares, Modeling of degradation by impact of individual iron ore pellets, Powder Technol. 378 (2021) 795–807.

[48] A.D. Salman, C.A. Biggs, J. Fu, I. Angyal, M. Szabó, M.J. Hounslow, An experimental investigation of particle fragmentation using single particle impact studies, Powder Technol. 128 (2002) 36–46.

[49] D.G. Papadopoulos, Impact Breakage of Particulate Solids, Ph.D. Thesis, University of Surrey, 1998.

[50] W. Goldsmith, Impact: The Theory and Practical Behaviour of Colliding Solids, Edward Arnold, London, 1960.

[51] D.A. Hills, D. Nowell, A. Sackfield, Mechanics of Elastic Contacts, Butterworth-Heinemann, Oxford, 1993.

[52] K.L. Johnson, Contact Mechanics, Cambridge University Press, 1985.